NREL
NATIONAL RENEWABLE ENERGY LABORATORY

Comparison of Photoluminescence Imaging on Starting Multi-Crystalline Silicon Wafers to Finished Cell Performance

Preprint

Steve Johnston, Fei Yan, Mowafak Al-Jassim
National Renewable Energy Laboratory

David Dorn
Specialized Imaging

Katherine Zaunbrecher
National Renewable Energy Laboratory and Colorado State University

Omar Sidelkheir and Kamel Ounadjela
Calisolar

Presented at the 2012 IEEE Photovoltaic Specialists Conference
Austin, Texas
June 3–8, 2012

NREL is a national laboratory of the U.S. Department of Energy, Office of Energy Efficiency & Renewable Energy, operated by the Alliance for Sustainable Energy, LLC.

Conference Paper
NREL/CP-5200-54113
June 2012

Contract No. DE-AC36-08GO28308

NOTICE

The submitted manuscript has been offered by an employee of the Alliance for Sustainable Energy, LLC (Alliance), a contractor of the US Government under Contract No. DE-AC36-08GO28308. Accordingly, the US Government and Alliance retain a nonexclusive royalty-free license to publish or reproduce the published form of this contribution, or allow others to do so, for US Government purposes.

This report was prepared as an account of work sponsored by an agency of the United States government. Neither the United States government nor any agency thereof, nor any of their employees, makes any warranty, express or implied, or assumes any legal liability or responsibility for the accuracy, completeness, or usefulness of any information, apparatus, product, or process disclosed, or represents that its use would not infringe privately owned rights. Reference herein to any specific commercial product, process, or service by trade name, trademark, manufacturer, or otherwise does not necessarily constitute or imply its endorsement, recommendation, or favoring by the United States government or any agency thereof. The views and opinions of authors expressed herein do not necessarily state or reflect those of the United States government or any agency thereof.

Available electronically at http://www.osti.gov/bridge

Available for a processing fee to U.S. Department of Energy
and its contractors, in paper, from:

U.S. Department of Energy
Office of Scientific and Technical Information

P.O. Box 62
Oak Ridge, TN 37831-0062
phone: 865.576.8401
fax: 865.576.5728
email: mailto:reports@adonis.osti.gov

Available for sale to the public, in paper, from:

U.S. Department of Commerce
National Technical Information Service
5285 Port Royal Road
Springfield, VA 22161
phone: 800.553.6847
fax: 703.605.6900
email: orders@ntis.fedworld.gov
online ordering: http://www.ntis.gov/help/ordermethods.aspx

Cover Photos: (left to right) PIX 16416, PIX 17423, PIX 16560, PIX 17613, PIX 17436, PIX 17721

Printed on paper containing at least 50% wastepaper, including 10% post consumer waste.

Comparison of Photoluminescence Imaging on Starting Multi-Crystalline Silicon Wafers to Finished Cell Performance

Steve Johnston, [1] Fei Yan,[1] David Dorn,[2] Katherine Zaunbrecher,[1,3] Mowafak Al-Jassim,[1] Omar Sidelkheir,[4] and Kamel Ounadjela[4]

[1]National Renewable Energy Laboratory; 15013 Denver West Parkway; Golden, CO 80401, USA
[2]Specialized Imaging; 3553 Clydesdale Parkway, Loveland, CO 80538, USA
[3]Colorado State University; Fort Collins, CO 80526, USA
[4]Calisolar; 985 Almanor Ave.; Sunnyvale, CA 94085, USA

***Abstract* — Photoluminescence (PL) imaging techniques can be applied to multicrystalline silicon wafers throughout the manufacturing process. Both band-to-band PL and defect-band emissions, which are longer-wavelength emissions from sub-bandgap transitions, are used to characterize wafer quality and defect content on starting multicrystalline silicon wafers and neighboring wafers processed at each step through completion of finished cells. Both PL imaging techniques spatially highlight defect regions that represent dislocations and defect clusters. The relative intensities of these imaged defect regions change with processing. Band-to-band PL on wafers in the later steps of processing shows good correlation to cell quality and performance. The defect band images show regions that change relative intensity through processing, and better correlation to cell efficiency and reverse-bias breakdown is more evident at the starting wafer stage as opposed to later process steps. We show that thermal processing in the 200°–400°C range causes impurities to diffuse to different defect regions, changing their relative defect band emissions.**

***Index Terms* — photoluminescence, imaging, infrared imaging, photovoltaic cells, silicon, impurities.**

I. Introduction

Imaging techniques can rapidly characterize material quality and defect density. Photoluminescence (PL) imaging can be applied to silicon from the brick level to all wafer process steps [1–8]. At the as-cut wafer stage, where thin, unpassivated wafers prevent accurate minority-carrier lifetime assessment due to surfaces, defects can still dominate recombination and can be categorized and quantified to predict finished cell performance [3–5]. Defect regions can be identified by recombination-limited band-to-band PL or by defect-band emission [9–18].

II. Experiment

A. Photoluminescence Imaging

We have used PL imaging as a measurement tool for characterization of starting multicrystalline silicon wafers and solar cells. Sets of neighboring wafers have been processed together with one from the set being pulled out after each process. We can then perform imaging on wafers from various ingot positions and at every process step. We have used a Princeton Instruments PIXIS 1024BR Si-charge-coupled-device camera with sensitivity out into the near-infrared (~1100 nm) for band-to-band PL imaging. An example of band-to-band PL imaging at all process steps is shown in the top row of Fig. 1. Bright regions correspond to good material quality, whereas dark regions are

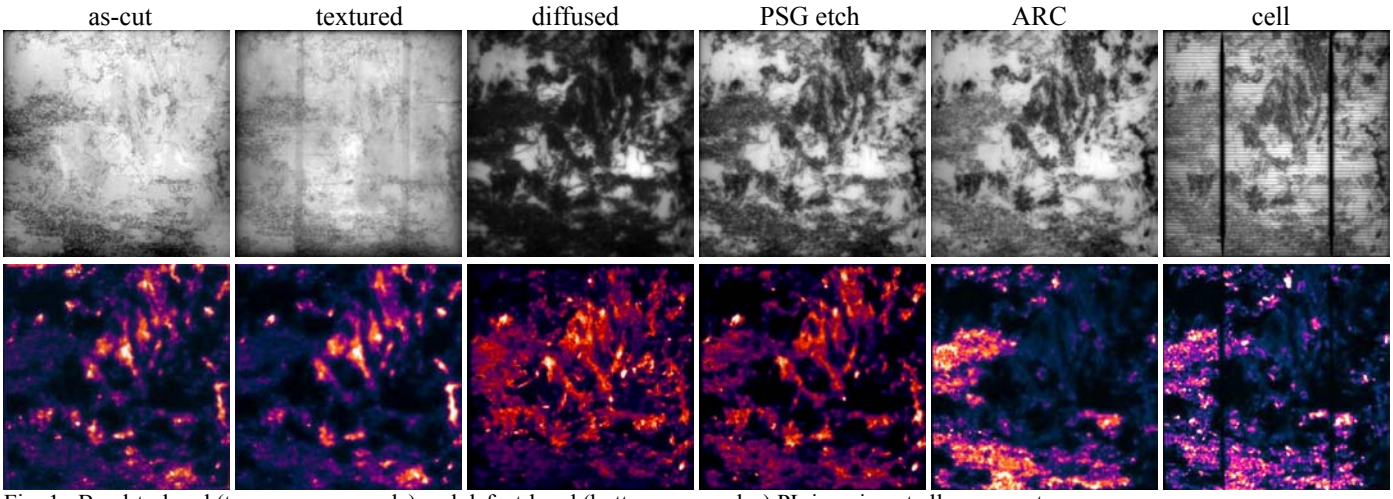

Fig. 1. Band-to-band (top row, gray-scale) and defect-band (bottom row, color) PL imaging at all process steps.

dominated by high carrier recombination due to defects and impurities. Starting wafers (as-cut and textured steps) are not passivated, and so, surface recombination limits radiative recombination of carriers. Here, the PL signal is weak and shows less contrast than later process steps. For these two wafers, defect regions on the left and bottom appear to be the darkest. At the diffusion step, the good-quality material has relatively very strong PL. To prevent saturation of the image at the bright locations, the image scaling makes defect areas appear larger. Once the phosphosilicate glass (PSG) is etched and removed, some surface passivation is lost and the PL signal is reduced. This reduces the range of PL across the sample and the image can be scaled to show higher-quality regions and defect regions with more clarity. The band-to-band PL then only shows subtle changes after the PSG removal to the antireflection coating (ARC) and finished cell process steps.

Defect-band emissions are imaged using a FLIR SC2500N InGaAs camera with lock-in data acquisition and sensitivity out to ~1700 nm. A long-pass filter (~1350 nm) is used to block band-to-band emissions. Examples of defect band emissions at all process steps are shown in the bottom row of Fig. 1. The defect-band images tend to initially highlight different regions when compared to the starting wafer band-to-band PL images. Then, the defect-band imaging changes contrast after the silicon-nitride ARC deposition. Regions that are dominantly bright in the as-cut and textured steps become relatively dim after ARC. Conversely, regions that are dim on the starting wafer become dominantly bright after ARC.

To determine which of these types of defect areas is more detrimental to cell performance, a light-beam induced current (LBIC) measurement was mapped on the finished cell. We have used a Semilab system for the LBIC measurement. The mapping resolution was set at a step size of 250 μm. The diffusion length was calculated based on internal quantum efficiencies using excitation light with wavelengths of 1014, 949, and 850 nm. The resulting diffusion length map is shown in Fig. 2. The areas shown in red have the lowest diffusion length and low quantum efficiencies when measured by the longer excitation wavelengths. These poorest performance areas correlate very well to the band-to-band PL image of the finished cell, as was shown in Fig. 1.

Image correlation of a starting wafer to the final cell would ideally provide information for predicting performance before the wafer is processed. Figure 3 shows comparisons of the as-cut wafer's band-to-band PL imaging and defect-band imaging to the finished cell's diffusion length map. The top row of images show the as-cut wafer's band-to-band PL image (left) compared to the diffusion-length map (right). The darkest areas of the as-cut wafer's PL image appear on the left side and bottom edge areas of the wafer. These same regions are somewhat dark on the diffusion length map. However, the diffusion-length map shows the darkest areas located in the

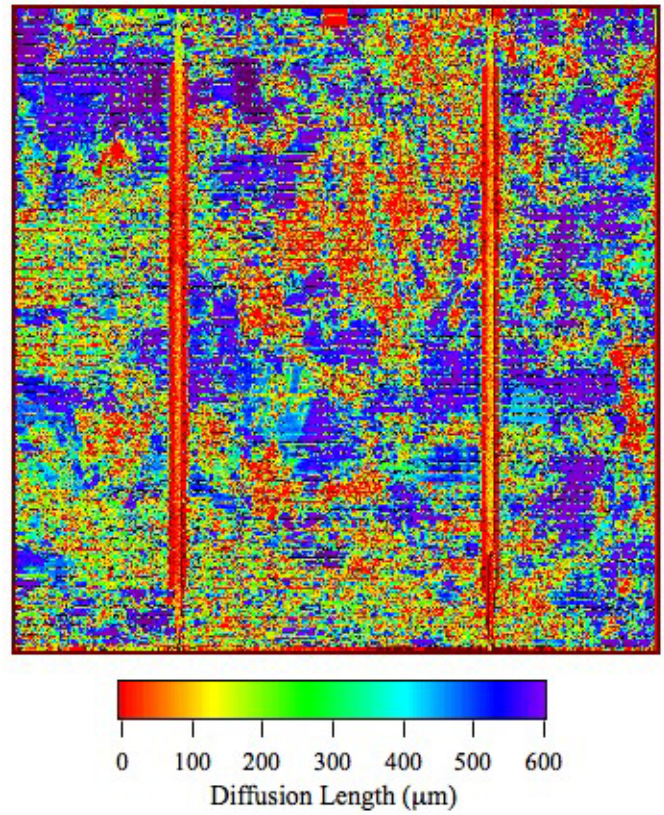

Fig. 2. Diffusion-length map of the finished cell from Fig. 1. Diffusion length is fit using Semilab LBIC data.

middle of the cell extending toward the upper right corner. In contrast to band-to-band PL, the as-cut wafer's defect-band image (lower left color image of Fig. 3) does show these areas to have the brightest defect-band emission. For ease of comparison, the diffusion-length map is inverted and plotted using the same color palette (lower right image of Fig. 3), and there is good correlation between the highest-emitting defect-band regions on the as-cut wafer and the poorest diffusion-length regions of the finished cell (bright due to inverted image). These imaging trends have been seen on wafer sets made from both upgraded metallurgical-grade (UMG) silicon and electronic-grade silicon.

B. Dark Lock-In Thermography

Dark lock-in thermography (DLIT) [19–22] is used to characterize the reverse-bias breakdown regions of the cell, as shown in Fig. 4. Defect-related breakdown, or stage II/type 2 breakdown, occurs roughly around 7 to 13 V reverse bias and has been associated with metallic precipitates in recombination-active regions [21, 23]. At voltages up to 13 V_{rev}, this defect-related breakdown leads to currents that increase quickly. Early breakdown, also called stage I/type 1 breakdown, is more linear and current begins to flow at smaller reverse biases. These defects are more likely related to cell processing and defects like surface cracks, metal paste

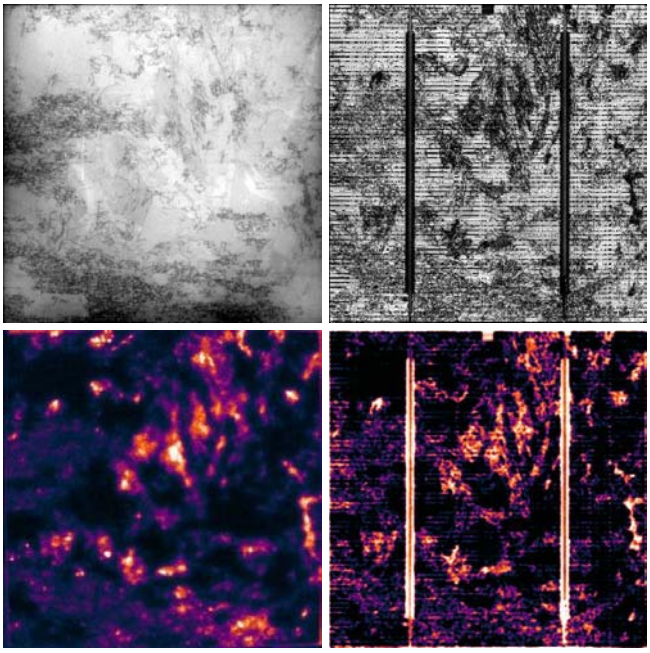

Fig. 3. As-cut wafer images are compared to the measured diffusion-length map of the finished cell from Fig. 1. The top row (gray-scale images) compares the band-to-band PL image of the as-cut wafer (left) to the finished cell's diffusion-length map (right). The bottom row (color) compares the defect-band PL image of the as-cut wafer (left) to the cell's diffusion-length map (right). Here, the diffusion-length map has been inverted (bright regions represent short diffusion lengths) and plotted using the same color palette as the defect band for ease of comparison.

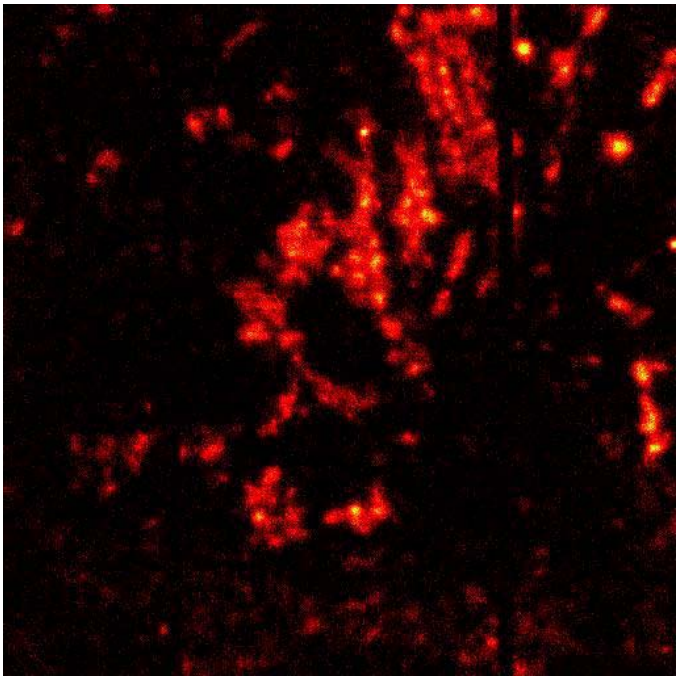

Fig. 4. Lock-in thermography image (slope-DLIT centered at 13 V_{rev}) of the finished cell from Fig. 1.

particles, and nonuniform firing of gridlines. To disregard the thermal signal from the early-breakdown, process-related defects and better emphasize the defect-related breakdown regions, we use slope-DLIT [21]. Here, the reverse bias is pulsed between 12.9 and 13.1 V_{rev}. At these biases around 13 V_{rev}, the defect-related breakdown currents are increasing most quickly. The weaker early-breakdown regions have currents that increase less in this voltage range, and this tends to then exclude the shunts that might otherwise appear strong, but that are more linear and not breaking down so quickly. In the cell's slope-DLIT image, the red areas show the regions that are heating due to flowing breakdown current. These defect-related breakdown areas show a very similar pattern to the poor diffusion-length areas that were shown in Fig. 2. Then, as compared before in Fig. 3, the as-cut defect-band image shows better spatial correlation to these areas than the as-cut band-to-band PL image. Thus, the as-cut wafer's defect-band image compares very well to both the breakdown regions of the DLIT image and the poorest-performance regions of the finished cell as measured by LBIC.

C. Defect-Band Process-Related Transition

In dozens of sample sets of both electronic-grade and upgraded metallurgical-grade, or solar-grade, multicrystalline silicon, we have consistently seen a change in the defect-band image's pattern at the silicon-nitride ARC processing step. An example was shown in Fig. 1, in which the wafers were from an electronic-grade silicon casting. The dominant defect-band emitting areas seem to switch at the ARC step. This leads to a better spatial correlation of defect areas when comparing the as-cut or textured wafer to the finished cell. But, because of the changing intensity ratios of these defect regions, the defect-band images do not show good correlation when comparing the finished cell's defect-band emission image to the same finished cell's performance and reverse-bias breakdown areas.

To better understand the relative switch in defect-band intensity at various defect regions, we have performed some additional experiments. Here, we have used a set of neighboring wafers from a UMG cast ingot. A ~5-cm-diameter region was laser cut from the PSG-etched wafer due to size limitations of the small furnace used for heat treatments. A series of heat treatments was performed on this cut-out wafer piece. Before each defect-band image acquisition, the wafer piece was etched in ~5% HF to improve surface passivation for better imaging.

The sample's initial defect-band PL image is shown in Fig. 5. Red ovals are drawn around various regions that begin with bright defect-band emissions at this PSG-etch process step. Green circles identify areas that begin with relatively low defect-band emissions. This sample is then placed in a small atmospheric furnace at 200°C for one hour. The sample is removed from the furnace, cooled with blown nitrogen, dipped in ~5% HF for a few minutes, and then imaged. The sample is then put in the 200°C furnace for an additional hour, and the

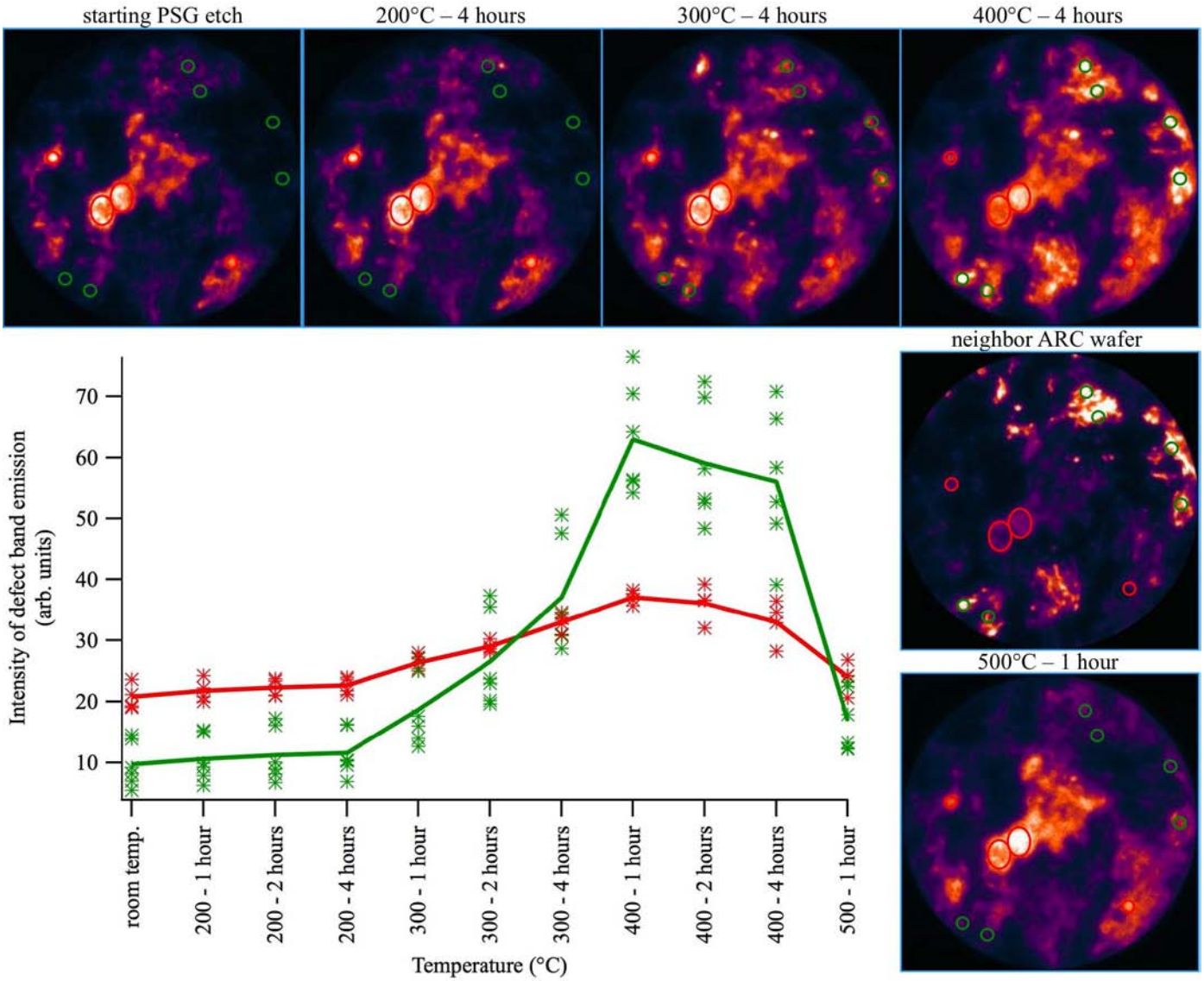

Fig. 5. Defect-band PL imaging of a ~5-cm-diameter circular cutout from a PSG-etched wafer is shown. The top row of images shows the starting defect-band image and images after 4 hours of accumulated heating at the labeled temperatures. The middle image on the right shows the defect-band image of the same region of the neighboring ARC-processed wafer. The bottom image shows the PSG-etched wafer after heating to 500°C for an hour. The graph shows the average defect-band intensity values with the labeled red and green areas of the PSG-etched wafer piece.

imaging is repeated. Finally, the sample is heated for two more hours, giving a total of four hours at 200°C. The image after four cumulative hours at 200°C is shown in Fig. 5. Only small changes are visible.

The heating periods and imaging steps are repeated at 300°C and 400°C. At 300°C, changes in the defect-band emission are becoming more evident, as shown in Fig. 5. The regions marked by green circles are beginning to emit in the defect band. By 400°C, these green circle regions have become the dominant signals, and this sample's defect-band image is approaching that of the same region in the neighboring wafer that was processed through ARC, also shown in Fig. 5. To show how the intensities are changing, the average intensities of the areas within the red and green ovals are plotted in the graph of Fig. 5. It is shown that the areas marked in red begin with higher intensity and continue to become brighter with heating through the first hour at 400°C. The areas marked in green increase in intensity more quickly during the same heating range. With more time at 400°C, the defect-band emissions of both types of areas start to slightly decrease, and with just one hour of heating at 500°C, the defect band emissions revert back toward their initial appearance, as shown in Fig. 5. These heating temperatures of 300-400°C give evidence of the thermal energy needed to allow impurities to continue to accumulate at the extended defects, which include dislocations and stacking

faults. The actual ARC deposition comprises 30 minutes at 450°C. Temperatures of 500°C provide thermal energy that apparently allows impurities to redistribute throughout the material again.

As seen with wafer-scale PL imaging, two rather distinct types of defect regions of the wafer are observed. One shows bright defect-band emissions on the starting wafer that become relatively dim after ARC and on the finished cell. Conversely, the other shows dim defect-band emissions on the starting wafer, and these same areas appear the brightest after ARC and on the finished cell. Examples of each of these types of areas are shown on neighboring UMG silicon wafers in Fig. 6.

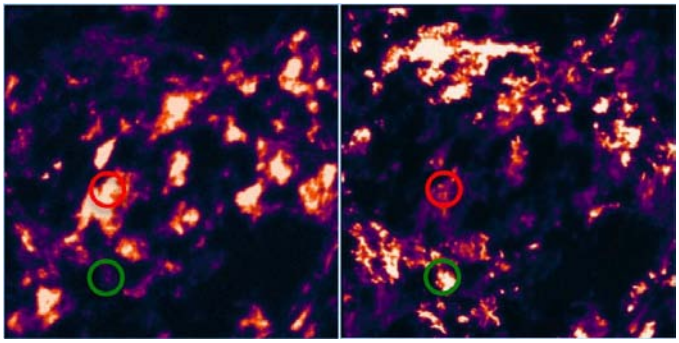

As-cut wafer ARC

Fig. 6. Defect-band imaging on a starting wafer and a neighboring wafer processed through the ARC step. The red-circled area shows a region that begins with high intensity and becomes relatively dim. The green-circled area shows a region with little defect-band emission on the starting wafer, but then becomes relatively bright at the ARC step.

Within the wafers shown in Fig. 6, there are many regions that demonstrate change in relative defect-band emission. We have selected a few of these regions for higher-resolution imaging. One example of the regions of the wafer whose defect-band emissions change contrast (circled areas from Fig. 6) is shown in Fig. 7. The top row shows room-light images of these 1-cm-diameter regions. The zoomed-in band-to-band PL images of these regions from the starting wafer are shown in the middle row. The areas that begin with brighter defect-band emission have relatively high dislocation/defect density, and the images from this region are outlined in red, as they were in Fig. 6. The region of Fig. 7 that is outlined in green begins with weaker defect-band emissions; but after ARC, this area has the more dominant defect-band emission. These regions tend to have a relatively lower dislocation/defect density. Lastly, the bottom row of images in Fig. 7 shows the defect-band emissions of the same regions from the ARC-processed neighboring wafer. As was presented in Figs. 1 and 6, full-wafer-sized defect-band images show large regions that switch relative intensity from starting wafer to the ARC step. When zooming into these regions, as highlighted by red and green circles in Fig. 6, higher-resolution images show that

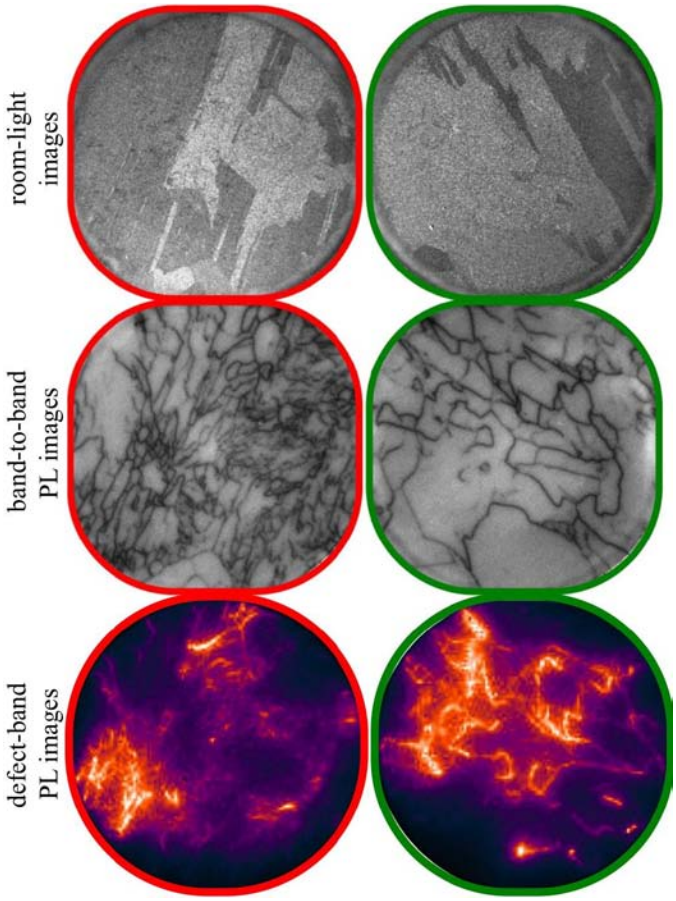

Fig. 7. Room-light (top row), band-to-band PL (middle row), and defect-band PL (bottom row) images of two 1-cm-size areas from the sample shown in Fig. 6. The sample outlined in red shows higher-intensity defect-band emissions at the starting wafer steps. The sample outlined in green begins with weaker defect-band emissions but has relatively brighter defect-band emissions after the ARC process and at the finished cell level. The band-to-band images are from the starting wafer, and the defect-band images are acquired at 78K from the same regions of the ARC-processed neighboring wafer.

these predominantly bright-to-dim or dim-to-bright regions are made up of smaller sub-regions that also change relative defect-band intensity between the starting wafer and the ARC processing step.

III. Conclusion

Both band-to-band and defect-band PL imaging have been applied at all processing steps of a multicrystalline Si solar cell. The finished cell's good- and poor-performing regions correlate well to the band-to-band PL image of the finished cell. However, these same spatial regions were better matched on the starting wafer by their defect-band emission. We have shown that the defect-band images on the starting wafer identified defect regions that correlated very well to the finished cell diffusion-length map and the reverse-bias

breakdown regions identified by slope-DLIT. Defect-band emissions have consistently shown regions that switch relative intensity between the starting wafer and the ARC processing step. We have shown that heating at ~300°C apparently allows impurities to continue to accumulate at dislocations and increase defect-band emissions, with some lower defect-density regions increasing defect-band emissions more quickly than higher defect-density regions. The defect-band images thus tend to highlight different regions when comparing the starting wafer to the ARC-processed wafer and finished cell. Consequently, the starting wafer's defect-band image better correlates to the finished cell's poor-performing regions.

ACKNOWLEDGEMENT

This work was supported by the U.S. Department of Energy under Contract No. DE-AC36-08GO28308 with the National Renewable Energy Laboratory and with support from the American Recovery and Reinvestment Act.

REFERENCES

[1] T. Trupke, R. A. Bardos, M. C. Schubert, and W. Warta, "Photoluminescence imaging of silicon wafers," *Appl. Phys. Lett.* **89**, 2006, 044107.

[2] T. Trupke, R. A. Bardos, M. D. Abbott, F. W. Chen, J. E. Cotter, and A. Lorenz, "Fast photoluminescence imaging of silicon wafers," *32nd IEEE PVSC* and *WCPEC-4*, 2006, pp. 928-931.

[3] W. McMillan, T. Trupke, J. W. Weber, M. Wagner, U. Mareck, Y. C. Chou, and J. Wong, "In-line monitoring of electrical wafer quality using photoluminescence imaging," *25th EPVSEC/5th WCPEC*, Valencia, Spain, 2010, pp. 1346-1351.

[4] J. Haunschild, M. Glatthaar, M. Demant, J. Nievendick, M. Motzko, S. Rein, and E. R. Weber, "Quality control of as-cut multicrystalline silicon wafers using photoluminescence imaging for solar cell production," *Sol. Ener. Mat. & Sol. Cells* **94**, 2010, pp. 2007-2012.

[5] T. Trupke, J. Nyhus, and J. Haunschild, "Luminescence imaging for inline characterization in silicon photovoltaics," *Phys. Status Solidi RRL* **5**, 2011, pp. 131-137.

[6] T. Trupke, J. Nyhus, R. A. Sinton, and J. W. Weber, "Photoluminescence imaging on silicon bricks," *Proceedings of the 24th European Photovoltaic Solar Energy Conference*, Hamburg, Germany, 2009, pp. 1029-1033.

[7] B. Mitchell, T. Trupke, J. W. Weber, and J. Nyhus, "Bulk minority carrier lifetimes and doping of silicon bricks from photoluminescence intensity ratios," *J. Appl. Phys.* **109**, 2011, 083111.

[8] J. Haunschild, M. Glatthaar, S. Riepe, and S. Rein, "Quality control using luminescence imaging in production of mc-silicon solar cells from UMG feedstock," in *35th IEEE PVSC*, 2010, pp. 812-816.

[9] I. Tarasov, S. Ostapenko, C. Haessler, and E. U. Reisner, "Spatially resolved defect diagnostics in multicrystalline silicon for solar cells," *Mat. Sci. & Engr. B* **71** (1-3), 51-55 (2000).

[10] M. Kittler, W. Seifert, T. Arguirov, I. Tarasov, and S. Ostapenko, "Room-temperature luminescence and electron-beam-induced current (EBIC) recombination behaviour of crystal defects in multicrystalline silicon," *Sol. Ener. Mat. & Sol. Cells* **72**, 2002, pp. 465-472.

[11] M. Kasemann, W. Kwapil, M. C. Schubert, H. Habenicht, B. Walter, M. The, S. Kontermann, S. Rein, O. Breitenstein, J. Bauer, A. Lotnyk, B. Michl, H. Nagel, A. Schutt, J. Carstensen, H. Foll, T. Trupke, Y. Augarten, H. Kampwerth, R. A. Bardos, S. Pingel, J. Berghold, W. Warta, and S. W. Glunz, "Spatially resolved silicon solar cell characterization using infrared imaging methods," in *33rd IEEE PVSC*, 2008.

[12] F. Dreckschmidt, H. Fiedler, D. Kreßner-Kiel, and H. J. Möller, "Sub-bandgap electroluminescence at room temperature of extended defects in multicrystalline silicon," *Proceedings of the 23rd European Photovoltaic Solar Energy Conference*, Valencia, Spain, 2008, pp. 407-410.

[13] K. Bothe, K. Ramspeck, D. Hinken, C. Schinke, J. Schmidt, S. Herlufsen, R. Brendel, J. Bauer, J.-M. Wagner, N. Zakharov, and O. Breitenstein, "Luminescence emission from forward- and reverse-biased multicrystalline silicon solar cells," *J. Appl. Phys.* **106**, 2009, 104510.

[14] P. Gundel, M. C. Schubert, and W. Warta, "Simultaneous stress and defect luminescence study on silicon," *Phys. Status Solidi A* **207**, 2010, pp. 436-441.

[15] M. C. Schubert, W. Kwapil, J. Schon, H. Habenicht, M. Kasemann, P. Gundel, M. Blazek, and W. Warta, "Analysis of performance limiting material properties of multicrystalline silicon," *Sol. Ener. Mat. & Sol. Cells* **94**, 2010, pp. 1451-1456.

[16] M. P. Peloso, P. Chaturvedi, P. Wurfel, B. Hoex, and A. G. Aberle, "Observations on the Spectral Characteristics of Defect Luminescence of Silicon Wafer Solar Cells," in *35th IEEE Photovoltaic Specialists Conference*, 2010, pp. 2714-2717.

[17] R. P. Schmid, D. Mankovics, T. Arguirov, M. Ratzke, T. Mchedlidze, and M. Kittler, "Rapid dislocation-related D1-photoluminescence imaging of multicrystalline Si wafers at room temperature," *Phys. Status Solidi A* **208**, 2011, pp. 888-892.

[18] F. Yan, S. Johnston, K. Zaunbrecher, M. Al-Jassim, O. Sidelkheir, and K. Ounadjela, "Defect-band photoluminescence imaging on multi-crystalline silicon wafers," *Phys. Status Solidi RRL* **6**, 2012, pp. 190-192.

[19] O. Breitenstein, M. Langenkamp, O. Lang, and A. Schirrmacher, "Shunts due to laser scribing of solar cells evaluated by highly sensitive lock-in thermography," *Sol. Ener. Mat. & Sol. Cells* **65**, 2001, pp. 55-62.

[20] O. Breitenstein, J. Bauer, J.-M. Wagner, and A. Lotnyk, "Imaging physical parameters of pre-breakdown sites by lock-in thermography techniques," *Prog. Photovolt: Res. Appl.* **16**, 2008, pp. 679-685.

[21] O. Breitenstein, J. Bauer, J. –M. Wagner, H. Blumtritt, A. Lotnyk, M. Kasemann, W. Kwapil, and W. Warta, "Physical mechanisms of breakdown in multicrystalline silicon solar cells," in *34th IEEE PVSC*, Philadelphia, PA (2009).

[22] O. Breitenstein, W. Warta, and M. Langenkamp, *Lock-in Thermography: Basics and Use for Evaluating Electronic Devices and Materials*, 2nd ed., Springer-Verlag, Berlin, 2010.

[23] W. Kwapil, J. Nievendick, A. Zuschlag, P. Gundel, M. C. Schubert, and W. Warta, "Influence of surface texture on the defect-induced breakdown behavior of multicrystalline silicon solar cells," *Prog. Photovolt: Res. Appl.* (2012).